

# An Adaptive Signal Photon Detection Method Based on DBSCAN for Photon-Counting Laser Altimeter

Xiangfeng Liu , Zhenhua Wang , Wuzhong Yang , Shixian Chen , Fengxiang Wang , Xiaowei Chen ,  
Weiming Xu , and Rong Shu 

**Abstract**—Photon-counting light detection and ranging is very sensitive to ambient interference, target features, and instrument performance, especially for long-distance detection of spaceborne laser altimeter and measurement of complex land-cover types with steep terrain. It is crucial to extract the signal photons on the ground surface from the collected photon point cloud (PPC). An adaptive signal photon detection method is presented in this article, which combines histogram statistics and boxplot analysis with density-based spatial clustering of applications with noise (DBSCAN), to denoise the PPC data with strong and weak noise obtained by ice, cloud, and land elevation satellite-2 laser altimeter. First, a coarse denoising with histogram of elevation is conducted on the raw PPC to reduce the calculation amount. Second, a fine denoising based on adaptive DBSCAN is used to extract the signal photons, where the key parameters of elliptic filter kernel are automatically determined according to the topographic data situation. We compared it with other methods, including local distance statistics (LDS), traditional and modified DBSCAN, traditional and modified ordering points to identify cluster structure (OPTICS), and ATL08 data. Some quantitative indicators, such as recall (R), precision (P), and F-score (F), are used to evaluate its performance. The results show that; 1) the adaptive DBSCAN has the best performance on preserving the vertical structural characteristics of ground objects, and 2) the adaptive DBSCAN in the mean R, P, and F of three land covers (i.e., mountain forest, urban, and water areas) can get up to the maximum are 0.9852, 0.9675, and 0.9761, respectively; followed by ATL08 data with 0.9773, 0.9412, and 0.9536, modified OPTICS with 0.9684, 0.9460, and 0.9586, and modified DBSCAN with 0.9613, 0.9474, and 0.9544; and then OPTICS with 0.9444, 0.9397, and 0.9378, and the DBSCAN with 0.9444, 0.9355, and 0.9554; the last one is LDS with 0.9382, 0.9261, and 0.9422. The proposed method provides an alternative approach for rapid and accurate processing of PPC on complex terrain.

**Index Terms**—Adaptive signal photon detection, denoising, density-based spatial clustering of applications with noise (DBSCAN), photon-counting laser altimeter, photon point cloud (PPC).

## I. INTRODUCTION

**L**IGHT detection and ranging (LiDAR) is an advanced remote sensing technology that enables three-dimensional (3-D) measurement of both natural and manmade terrain. This technology operates by emitting laser pulses from platforms, such as aircraft or satellite, receiving and measuring the time it takes for the signals to return from the object surface, and then calculating the elevation of the terrain below. It is extensively utilized for land planning and management, natural hazards monitoring, hydrology, and oceanography [1], [2]. Despite the numerous advantages of LiDAR technology, there is still a need to further improve the efficiency, accuracy, and resolution of the measurements while reducing the cost of platform resources and power consumption. Following the success of airborne test instrument, slope imaging multipolarization photon-counting LiDAR and multiple altimeter beam experimental LiDAR [3], [4], [5], the ice, cloud, and land elevation satellite-2 (ICESat-2) was launched on Sep. 15, 2018. It carried an advanced topographic laser altimeter system (ATLAS), which is the first spaceborne photon-counting laser altimeter. Compared to the traditional discrete-return and full waveform LiDAR with linear detection mechanism, such as shuttle laser altimeter, geoscience laser altimeter system, global ecosystem dynamics investigation, and China's ZiYuan-302 and Gaofen-7 laser altimetry, the single photon-counting LiDAR (PCL) has several advantages due to its more sensitive detector (Geiger mode avalanche photodiodes or photomultipliers). It comes with high sensitivity, high frequency, low energy, and low divergence, making it suitable for weak detection, harsh environments, complex and distant targets, and limited platform resources. It can meet multibeam requirements, provide dense along-track sampling, and offer high-resolution single-photon data [6], [7], [8], referred to as photon point cloud (PPC). The PCL is becoming increasingly popular because it can provide massive data and detect objects invisible to traditional remote sensing technologies. However, since this mechanism of PCL is sensitive to individual photon, it cannot only receive signal echoes reflected from the ground surface but also record noise echoes returned by scattering and reflection, thus its data can severely be affected by the ambient condition (atmospheric scattering and solar radiation), target feature (land-cover types

Manuscript received 19 October 2023; revised 14 December 2023; accepted 6 January 2024. Date of publication 10 January 2024; date of current version 29 January 2024. This work was supported in part by the Natural Science Foundation of Shanghai Municipality under Grant 23ZR1473200, and in part by the Key Laboratory of Space Active Opto-electronics Technology, Chinese Academy of Sciences (CAS) under Grant CXJJ-22S019. (Corresponding authors: Zhenhua Wang; Weiming Xu.)

Xiangfeng Liu and Fengxiang Wang are with the Key Laboratory of Space Active Opto-electronics Technology, CAS, Shanghai 20083, China, and also with the Shanghai Institute of Technical Physics (SITP), CAS, Shanghai 20083, China (e-mail: xiangfeng\_liu@163.com; wangfengxiang@mail.sitp.ac.cn).

Zhenhua Wang, Wuzhong Yang, and Shixian Chen are with the College of Information Technology, Shanghai Ocean University, Shanghai 201306, China (e-mail: zh-wang@shou.edu.cn; 563539827@qq.com; 751184523@qq.com).

Xiaowei Chen is with the Beijing Institute of Tracking and Telecommunications Technology, Beijing 100094, China (e-mail: chenxw\_2007@aliyun.com).

Weiming Xu and Rong Shu are with the Hangzhou Institute for Advanced Study, UCAS, Hangzhou 310024, China, and also with the Shanghai Institute of Technical Physics, CAS, Shanghai 20083, China (e-mail: xuwm@mail.sitp.ac.cn; shurong@mail.sitp.ac.cn).

Digital Object Identifier 10.1109/JSTARS.2024.3352023

and reflectance), and instrument performance (transmit energy, detector efficiency, and dead-time and after-pulsing effect) [9], [10]. As a result, there are usually numerous noise photon events randomly and widely distributed along the laser propagation path, especially in the daytime data. Therefore, denoising technology is needed to extract the signal photons of the ground surface from noisy PPC data, which is a critical process that directly affects the quality and usefulness of the data for subsequent applications, especially in complex area with steep terrain.

Because PPC data are characterized by concentrated signal photons and relatively discrete noise photons in the vertical versus horizontal distribution, and the ground surface is continuous, scholars have performed many supervised and unsupervised classification algorithms to extract signal photons. There are three typical methods as follows.

- 1) *Image processing or grid statistical filtering*: This method rasterizes the PPC along the track into 2-D images [11], [12], [13] or voxel grids [14] based on the density of photons. Image processing techniques are then used to identify signal photons, such as edge and region detection, probability distribution function, median filters, etc. However, this method may result in the loss of useful information during the transformation from photons to rasterized data.
- 2) *Histogram statistic or probability density*: This method involves analyzing the local density information and relative neighboring relationship in the spatial distribution of photons, using localized statistical analysis [15], [16], [17], [18], [19], [20], local angle mapping [12], local distance statistics (LDS) [21], local outlier factor (LOF) [22], spatial statistical and discrete mathematical concepts [23], and k-nearest neighbor or Bayesian decision [24] to identify the signal photons. However, this method lacks consideration for the influence of terrain slope and the problem of uneven density distribution of PPC data.
- 3) *Density clustering*: This method involves analyzing the spatial distribution information of PPC data to identify signal photons with a local cluster criterion, such as common and modified density-based spatial clustering of applications with noise (DBSCAN) [6], [25], [26], crisp clustering [11], and ordering points to identify the clustering structure (OPTICS) [27], [28]. It has been demonstrated that this is the most popular and effective method currently, however, it fails to effectively filter out noise photons in vegetated environments with steep terrain [11], [24]. Some multistage filtering algorithms have been proposed to solve the photon filtering problem from complex terrain. For example, Popescu et al. [11] proposed a multilevel filtering algorithm to remove the noise photons, and the signal photons, after filtering, were classified into ground and canopy using moving windows and cubic spline interpolation. Neumann et al. [29] used an ellipsoidal-based slant histograms to identify the signal photons over slope regions in the ATLAS ATL03 data product, which also performed in [30]. Neuenschwander and Pitts [31] used a differential, regressive, and Gaussian adaptive nearest neighbor (DRAGANN) to extract of terrain and canopy heights from the ATLAS

ATL03 data and generate the ATL08 data product. Xie et al. [32] conducted a review and comparison of the surface detection methods. For spaceborne laser altimetry, each detection task will obtain PPC data with a long along-track distance, which inevitably covers various land-cover types with complex terrains, including land, urban areas, forests, water bodies, and mountains. There are still great challenges to accurately extract the signal photons with an effective method, especially for the complex surfaces with large terrain variations and inconsistent strong and weak noise.

The density clustering methods have been demonstrated to have good performance, where a circle or an ellipse filtering kernel is usually used to analyze the neighbors of photons [33]. Thereinto, the DBSCAN, first introduced by Ester et al. [34], could efficiently cluster signal photons without target clusters and discover clusters of an arbitrary shape. In algorithm DBSCAN and similar algorithm OPTICS, the determination of the main parameters of the circular filter kernel, such as neighbor radius (Eps) and minimum number of neighbors points (MinPts), is a key factor that directly affects the denoising performance. The modified DBSCAN and OPTICS change the circular filter kernel into an ellipse [6], [19], [22], [25], [27], [35], [36], [37], [38], [39], which increases the weight of horizontal distance to be more suitable for signal identification of ground clustered photons, but it brings difficulties in setting more parameters, such as major and minor axes and direction. Currently, some strategies are used to automatically determine the main parameters of filtering kernel as follows.

- 1) *Respect to Eps and MinPts parameters*: Ma et al. [40] set a fixed radius (Eps) of DBSCAN according to the land type and determined the MinPts based on the photon number of signal and noise on the land-cover types in coastal area. Huang et al. [26] used a particle swarm optimization algorithm to optimize the two parameters. Zhang et al. [36] set the MinPts as three times of the noise rate. Meng et al. [41] used K-mean nearest neighbor to optimize the Eps and calculated an adaptive denoising threshold based on the sea surface data density.
- 2) *Respect to major and minor axes of ellipse*: Zhu et al. [19] set major and minor axes as specific values. Chen et al. [22] used an empirical ratio to set the major and minor axes. Zhang et al. [36] set the major and minor axes as the footprint diameter and receiving pulsewidth, respectively.
- 3) *Respect to filter direction*: Zhu et al. [19] and Xie et al. [35] adjusted the filter kernel direction with an angular interval to find the maximum photon number so that the filter kernel can optimally adapt to the local terrain slope. Zhang et al. [36] used the slope-noise relationship to rotate the direction of the searching neighborhood in the DBSCAN to obtain continuous terrain profile from the weak beam data. Lao et al. [37] and [38] employed random sample consensus (RANSAC) to find filter direction with the largest number of photons iteratively. He et al. [39] established the direction of elliptical search area of LOF according to the terrain slope of segment that calculated based on initial classification.

- 4) *Respect to threshold parameter*: Zhang et al. [42] adopted a genetic algorithm based on training data to select two parameters of localized statistics-based algorithm to calculate the distance sum and threshold to separate noise.

Most scholars count the density criterion of photons containing signal and noise and find the gap between them to distinguish the signal and noise photons. In a nutshell, the key parameters of filter kernel are almost manually determined according to the specific land-cover type, set by an empirical model, or optimized using prepared training dataset. Obviously, these are not convenient for fast and accurate processing of large regions covering different land-cover types and complex terrain, let alone meeting the needs of online processing. Therefore, it is inevitable to adopt adaptive unsupervised classification methods for the massive PPC data that cover multiple land-cover types simultaneously to select the optimal parameters.

To improve the denoising accuracy and keep more vertical structural information, an adaptive signal photon detection method for PPC data, while just considering the spatial distribution and density characteristics of PPC data, covering different land-cover types with different terrain slope, is demonstrated in this article. This method combines the histogram statistics and boxplot analysis with modified DBSCAN and adopts a two-step approach of coarse denoising and fine denoising. It employs an automated process to determine the main parameters, such as the size of the major and minor axes and direction of elliptical filter kernel, and MinPts parameter. It focuses on automatically determining the major and minor axes based on the density situation of PPC data to avoid the trouble of empirical models, and selecting directions according to the local terrain slope to avoid the high consumption of traversal search. Its performance is conducted on ATL03 data product of ICESat-2/ATLAS, and compared with other methods, including LDS, traditional and modified DBSCAN, traditional and modified OPTICS, and the results of ATL08 data.

The rest of this article is organized as follows. In Section II-A, the ATLAS instrument characteristics and experimental dataset are introduced. In Section II-B-1, a coarse denoising with Gaussian fitted histogram of elevation is described to extract the photons around the ground with a certain elevation window, to reduce the calculation amount of the raw data, and improve the operation efficiency. In Section II-B-2, a fine denoising based on adaptive DBSCAN is used to identify the signal photons on the ground surface, where the determination of the key parameters of modified DBSCAN is detailed. In Section II-C, some quantitative metrics are introduced to compare these methods, such as recall, precision, and F-score. In Section III, comparative experiments are conducted on strong and weak noise PPC data in mountain forest, urban, and water areas acquired by ATLAS, and the results and discussions are performed in detail. Finally, Section IV concludes this article.

## II. MATERIALS AND METHODS

### A. ICESat-2/ATLAS and Experimental Dataset

ICESat-2/ATLAS takes a 532-nm laser to emit a pulse, and each laser beam is split into six beams in cross-track direction

by a diffractive optical element (three pairs and each pair is consisted of a strong beam and a weak beam, where the energy of weak beams is approximately 1/4 compared to that of strong beams with  $45 \pm 5 \mu\text{J}$ ), the cross-track distance between adjacent strong beams is approximately 3.3 km and the distance between strong and weak beams of each pair is approximately 2.5 km [43]. The ATLAS uses a micropulse PCL operating at a high laser repetition rate of 10 kHz, generating more dense footprints in along-track direction with a diameter of  $\sim 17$  m separated by  $\sim 0.7$  m intervals along the ground track. The dense sampling of ATLAS allows an efficient measurement of the Earth's surface [8]. It also provides several data products to the science community and general public [44], including Level 1B (denoted as ATL02) to provide the time of flight, housekeeping data, and other data necessary for science data processing; Level 2A (identified as ATL03) to provide the latitude, longitude, and ellipsoidal height of photons recorded by the ATLAS; and the higher level surface-specific data products (named as Level 3A) generated based on the ATL03, which consist of glacier and ice sheet height, sea ice freeboard, vegetation canopy height, ocean surface topography, and inland water body height.

In the experiment, ATL03 datasets obtained from three detection tasks on Oct. 30, 2018, May 11, 2021 and May 28, 2021, respectively, and data from three strong beams in each task were selected for testing, containing the raw data points recorded with unique time tag, latitude, longitude, and WGS 84 ellipsoid elevation. The ATL08 datasets were also downloaded to help manually extracted signal photons on ground surface. Fig. 1 shows the ground tracks of geolocated PPC data, six tracks, locating at  $101\text{--}109^\circ\text{E}$  and  $33\text{--}51^\circ\text{N}$ , were collected in the daytime with high noise rate; while the other three tracks, locating at  $106\text{--}110^\circ\text{E}$  and  $32\text{--}37^\circ\text{N}$ , were collected at night with low noise rate. These tracks cover the mountain forest, urban, and water areas. Due to the lower transmitted laser energy, the mean signal photons per shot varied from 0.1 to 10 photons [8], [45]. The collected PPC from ground surface suffer from background noise, backscatter noise, detector dark noise, and after-pulsing noise. In the daytime, the solar background noise rate is approximately several MHz, making the number of background noise photons exceed the number of signal photons within the range gate. Compared to background noise, the detector dark noise rate is only several KHz and could be neglected [23]. The backscatter effect arising from clouds and aerosols and the after-pulsing detector effect introduce noise photons into the signal photons above and below the ground surface, respectively. As a result, the noise photons in daytime are much larger than that at night, resulting a lower signal–noise ratio in daytime, as shown by the large amount of noise in daytime in Fig. 1(a) and the small amount of noise at nighttime in Fig. 1(b). Nonetheless, the distribution of signal photons is more concentrated than the noise photons. The data of these tracks were detected by the strong beam in the experiment, since there was less noise in the weak beam recorded data.

### B. Adaptive Denoising of the Photon Point Cloud Data

The main workflow of this adaptive denoising method is shown in Fig. 2. First, a coarse denoising based on Gaussian

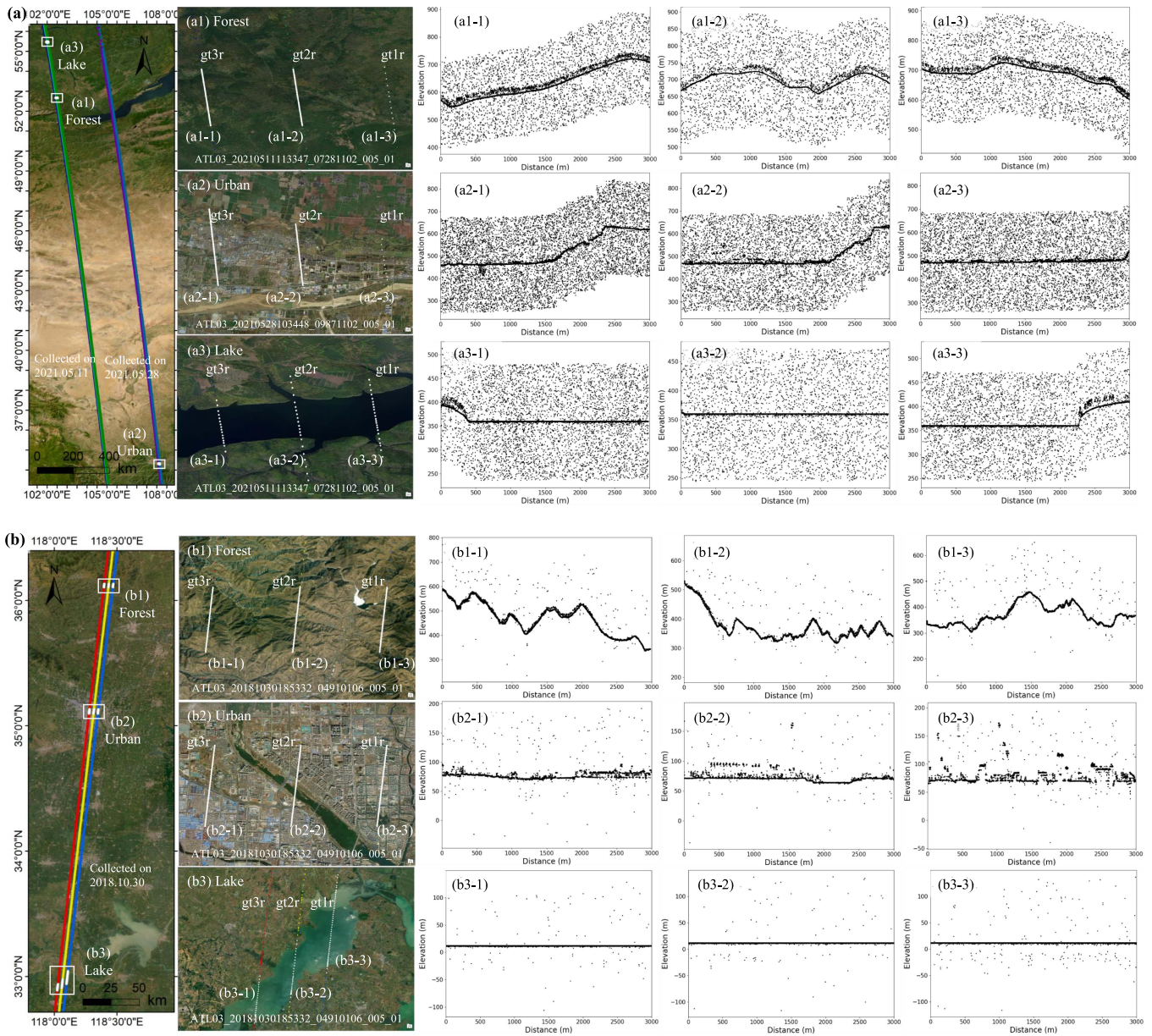


Fig. 1. Schematic diagram of photon point cloud and their ground tracks: (a) collected in the daytime (ATL03\_20210511113347\_07281102\_005\_01 and ATL03\_20210528103448\_09871102\_005\_01), and (b) collected at nighttime (ATL03\_20181030185332\_04910106\_005\_01).

fitting of elevation histogram is adopted to reduce the calculation amount of the raw data and improve the operation efficiency. That is, histogram statistics are made on the elevation of all photons in the PPC data according to the segmentation along-track distance, and then Gaussian function is used to fit the histogram and obtain the threshold that can remove the identified photons outside the terrain profile, i.e., preliminary noise photons. Second, a fine denoising based on modified DBSCAN is used to extract the signal photons on the objects surface, where the main parameters for the elliptic filter kernel and the denoising threshold are automatically determined according to the data distribution characteristics. In which, Gaussian fitting and boxplot analyses are used to analyze the clustering information of the remaining ground photons to help determine the major and

minor axes of the elliptic filter kernel of the DBSCAN, and then calculating the local slope using ground photons to determine the direction of the elliptic filter kernel. Finally, boxplot analyses are used to remove the abnormal points. All the processing steps were implemented using Python 3.6, and the details of each step are described as following sections.

*1) Coarse Denoising Based on Gaussian Fitting Histogram:* Although a certain range gate is set as the detection window during the PCL measurement, the PPC data still contain a large number of noises above and below the ground surface, which require further preprocessing to remove the background noise and reduce the amount of calculation. In the spaceborne PPC data, the density of signal photons reflected by the ground surface is usually two orders of magnitude greater than the atmospheric

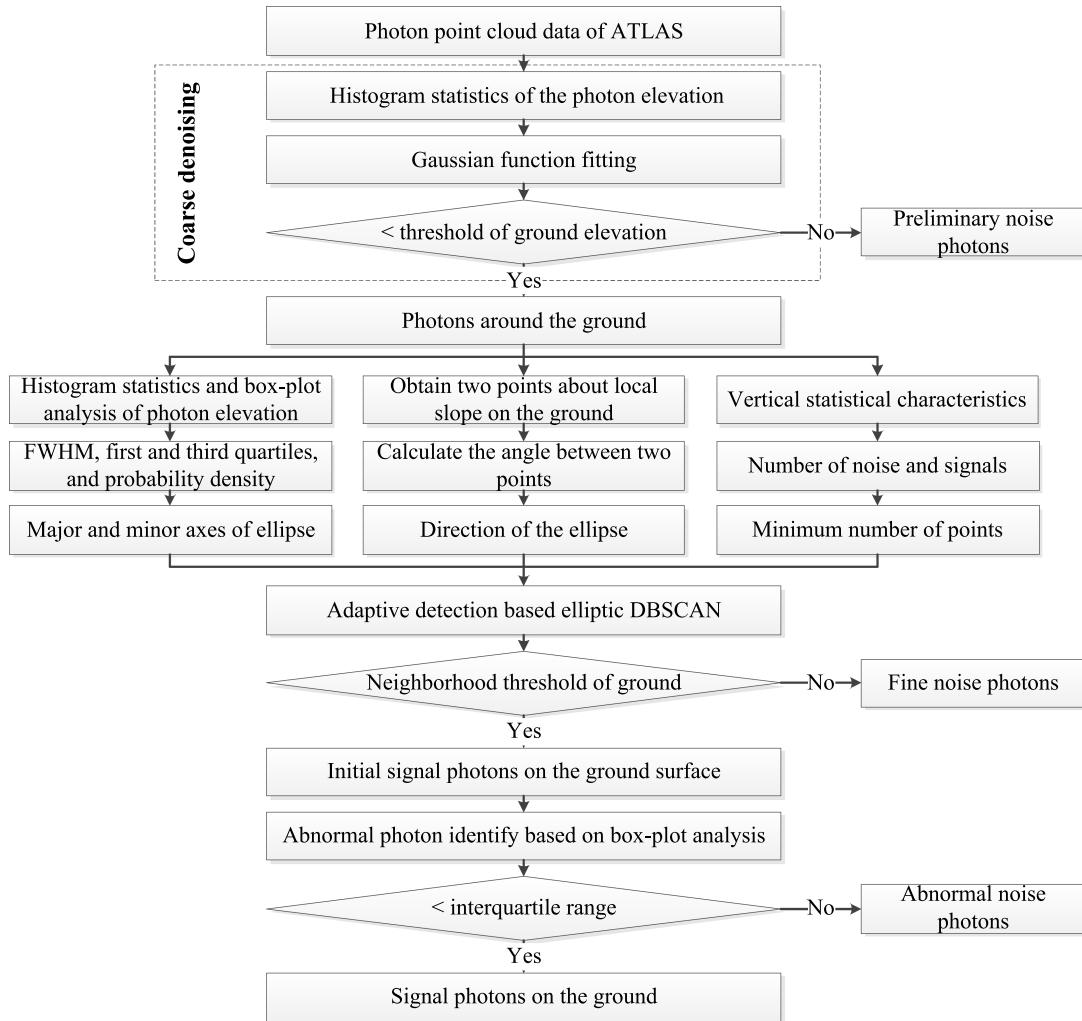


Fig. 2. Workflow of the adaptive denoising approach for photon-counting point cloud.

noise photons due to the performance of the single-photon detector and the influence by the laser energy and the solar radiation. Therefore, the histogram statistics of photon's elevation is likely to show a single-peak characteristics with low frequency on the left and right sides and high frequency in the middle, which can be fitted with a Gaussian function to obtain the threshold to remove pure background noise.

The main processing processes include the following conditions.

- Segmenting PPC data along-track distance with an interval of 100 m, which can be divided into Segment 1 to Segment  $n$ .
- Counting the number of photons within each elevation range with a bin of 10 m for each segmented data, so background photons in the histogram are randomly distributed in bins, while signal photons are clustered in one or a few bins.
- Calculating the elevation threshold of the initial signal photons by the distribution information of elevation and frequency in the histogram statistic, where the mean  $\mu$  and standard deviation  $\sigma$  of the elevation of signal photons'

distribution are fitted by a Gaussian function. Using the triple standard difference method, the upper and lower thresholds of ground elevation are set as  $\mu + t_1 \times \sigma$  and  $\mu - t_2 \times \sigma$ , respectively, and the value of  $t_1$  is twice that of  $t_2$  (i.e., 3 and 1.5, respectively), as the mean value is usually close to the ground surface and there are higher objects on the ground;

- Treating the photons within the threshold range as initial signal photons around the ground and the rest as preliminary noise photons.
  - Fine Denoising Based on Elliptic Filter Kernel DBSCAN:* Coarse denoising can remove over 90% of the background photons and preserve all photons around the ground, while fine denoising is needed to further identify and extract the signal photons on the ground surface, where the main parameters, such as major and minor axes, minimum number of neighbors points, and direction of elliptic filter kernel, should be automatically determined according to the PPC data distribution characteristics on land-cover types and terrain changes.
    - Automatic determination of the major and minor axes of the elliptic filter kernel:* After coarse denoising for noisy

photons, finer histogram statistics on the elevation of initial signal photons with a bin of 0.5 m for each segmented data along-track is conducted. To obtain a more refined elevation distribution range of PPC, the distribution characteristics of the ground photons is also fitted by a Gaussian function, such as half-height width (FWHM) and probability density. This parameter represents the elevation range of the ground surface and its land covers. Thus, the minor axes of elliptic filter kernel should be related to the elevation range, and the major axes should be correspondingly larger than the minor axes to increase the weight of horizontal distance, which is more suitable for signal identification of ground cluster photons. Generally, the steeper the terrain, the larger the elevation range of ground photons, and the wider of their FWHM. Then, we need to use a larger filter kernel. A boxplot analyses is introduced simultaneously based on the Gaussian fit value to determine the semi-minor axis  $b$  of the ellipse, where the first decision value  $b_1$  is calculated by Gaussian fitted FWHM, and the second decision value  $b_2$  is equal to the height difference between the first quartile  $Q_1$  and the third quartile  $Q_3$  of the boxplot. The semimajor axis of the ellipse can be determined by multiplying the probability density by the number of histograms  $n$

$$\text{FWHM} = 2\sqrt{\ln 2}\sigma \quad (1)$$

$$b_1 = \frac{1}{2} \sqrt{\text{FWHM}} \quad (2)$$

$$b_2 = Q_1 - Q_3 \quad (3)$$

$$b = \sqrt{b_1 \times b_2} \quad (4)$$

$$a = n \times \text{density} \quad (5)$$

where  $\sigma$  is the standard deviation of Gaussian fitting and density is the probability density of the frequency of the photons number.

*b) Automatic determination the optimal direction of the elliptic filter kernel:* When the circular filtering kernel is modified to an ellipse, the horizontal elliptic filter kernel does achieve good performance on flat terrain, but there are some limitations in mountainous areas, especially those with steep terrain. Due to densely distributed signal photons gathering on the topographic profile along the terrain slope, the optimal filter direction can obtain the largest number of photons and be consistent with the local terrain slope. Different from some current methods, such as traversing the PPC with specific angular intervals to find the direction with the largest photon density, evaluating the main direction of the photon distribution by principle component analysis, and extracting the largest number of photons and iteratively fitting model meeting the terrain slope by RANSAC. Our method directly calculates the local slope within the elliptic filter kernel. The neighbor distance between two points is calculated by

$$\text{Dist}(p, q) = \sqrt{\frac{\Delta X_\theta^2}{a^2} + \frac{\Delta H_\theta^2}{b^2}} \quad (6)$$

$$\begin{cases} \Delta X_\theta = \cos\theta (X_p - X_q) + \sin\theta (H_p - H_q) \\ \Delta H_\theta = \sin\theta (X_p - X_q) + \cos\theta (H_p - H_q) \end{cases} \quad (7)$$

$$\theta = \tan^{-1} \left( \frac{H_r - H_l}{X_r - X_l} \right) \quad (8)$$

where  $p$  and  $q$  are any two photons in the PPC data,  $a$ ,  $b$ , and  $\theta$  are semimajor and semiminor axes and direction of elliptic filter kernel, respectively;  $X_p$  and  $X_q$  are the along-track distance, respectively,  $H_p$  and  $H_q$  are the elevation of the two points, respectively. When  $\text{Dist}(p, q)$  is less than 1, it means the point is inside the elliptic filter kernel; otherwise, it means the point is outside the elliptic filter kernel. The direction of the elliptic filter kernel can be determined by calculating the angle for the ground photon on the left and right sides of the elliptical search area, as represented in (8), and that as the local terrain slope within the search area, where  $X_r$  and  $X_l$  are the right and left along-track distance, respectively, which can be determined based on the location of the elliptical search area; and  $H_r$  and  $H_l$  are the elevation of that on the ground profile, respectively, which need to be determined according to the photons' distribution density. In this article, the leftmost and rightmost boundaries of the elliptical search area are taken as the centers, and the size of half of semiminor axis is extended toward both sides, taking into account the high undulating terrain. Calculate the elevation values with the highest probability density within these two rectangular regions as the two elevation values.

*c) Automatic determination of the minimum number of points parameters:* The automatic calculation steps for this parameter refers to [40]; it is also briefly described here to maintain the completeness of this article. In the finer histogram statistics, the photons in each segment are evenly divided into  $M$  segments along the elevation, and the elevation bin can be expressed as  $h = R_g/M$ , where  $R_g$  is the elevation range. The average number of photons in all vertical segments is  $N_t/M$ , where  $N_t$  is the total number of photon points in this segment. Calculate the number of segments  $M_2$  with photon numbers less than the average number, and calculate the total photon number  $N_2$  in these segments. Then, the number of segments  $M_1$  with photon number greater than the average number is calculated, and the total number of photons is  $N_1 = N_t - N_2$ . For noise photons, the photon density per unit extended track distance and per unit elevation length  $\rho_2 = N_2/(h \times l \times M_2)$ . Similarly, for a mixture of signal and noise photons, photon density per unit along-track distance and per unit elevation length  $\rho_1 = N_1/(h \times l \times M_1)$ . Thus, for the two segments of  $M_1$  and  $M_2$ , the expected number of photons in the search kernel can be expressed as

$$SN_i = \rho_i \times S = \frac{\pi ab N_1}{hl M_i} \quad (9)$$

$$\text{MinPts} = \frac{2SN_1 - SN_2 + \ln(M_2)}{\ln\left(\frac{2SN_1}{SN_2}\right)} \quad (10)$$

Given the expected number of noise and signal photons in the neighborhood, the parameter MinPts can be expressed as (10).

Finally, there may be some abnormal photons within each segment. These can be analyzed by the boxplot, and the photons outside the interquartile range can be marked as the abnormal noise photons. And the final retained photons serve as the signal photons on the ground surface.

### C. Comparison and Evaluation of Denoising Performance

In order to evaluate the performance of this method across different land-cover types, we compared it with other methods including LDS [21], DBSCAN [34], modified DBSCAN [25], OPTICS [27], and modified OPTICS [28] using PPC data from the mountain, urban, and water areas. In addition, we also compared with the results of ATL08 data products (i.e., DRAGANN) by merging the classification results of land, water, vegetation, canopy, etc., in the data as signal photons. The LDS method calculates the total amount of the nearest neighbor distance between each point and surrounding points, counts the frequency of local total distance using a histogram, and fits with Gaussian function to obtain the threshold that can distinguish the signal from the noise. The DBSCAN method uses a circular filtering kernel to traverse all points within the neighborhood of each point, and takes the clusters with a number greater than MinPts as the signal. The OPTICS method is similar to DBSCAN, but instead of dividing the data into different blocks, it constructs a reachability graph for each point and assigns a distance reachability to each point and ordering in the cluster, and then determines the members of the cluster. The modified DBSCAN and OPTICS change the circular filter kernel into an ellipse. Referring to the ATL08 data, the manually extracted results from ATL03 data serve as the reference ground truth, in which all the noise photons are manually removed, leaving only real photon signals.

To quantitatively estimate the performance of these denoising algorithms, three indicators were evaluated using a reference data, including recall  $R$ , precision  $P$ , and the harmonic mean of recall and precision  $F$ -score. These three indicators are calculated using the reference classification data, and they are, respectively, given by

$$R = \frac{TP}{TP + FN} \quad (11)$$

$$P = \frac{TP}{TP + FP} \quad (12)$$

$$F = \frac{2 \times P \times R}{P + R} \quad (13)$$

where  $TP$ ,  $FP$ , and  $FN$  represent the number of correctly classified true signal photons, noise photons misclassified as signal photons, and true signal photons misclassified as noise photons, respectively. Thereinto,  $R$  denotes the ratio of signal photons that are successfully detected to all the true signal photons,  $P$  denotes the ratio of true signal photons that are correctly classified to all the detected signal photons, and  $F$  denotes the harmonic mean of recall and precision. The  $F$  value can indicate the effectiveness of the denoising algorithm, and the higher  $F$ -score shows a better effect.

## III. RESULT AND DISCUSSION

### A. Performance of the Signal Photon Detection in Multiple Ground Types

In the experiment, the adaptive DBSCAN was conducted on the ATL03 PPC data, covering mountain forest, urban, and water

areas with strong and weak noise. Based on the characteristics that signal photons are more concentrated than noise photons, the most densely distributed photon were selected as the core point, and then the adjacent points were searched from the core point for clustering. Photons beyond the clustering threshold were labeled as noise.

Fig. 3 shows the coarse and fine denoising results for the PPC data with strong and weak noise in the mountain forest, water, and urban area, where the coarse denoising results are displayed with blue dots and the fine denoising results are displayed with red dots. It can be seen that the noise photons in the periphery of signal photons have been removed from the PPC data after coarse denoising especially for the data with strong noise, and the remaining photons are composed of signal photons and some noise photons distributed near the ground surface along the terrain. The coarse denoising cannot only remove a large number of noise photons, but also greatly simplify the subsequent calculation. The noise photons on the surface of forest, buildings, and water are very close to the real signal photons and have a higher density than the surrounding noise photons, making them difficult to remove. So the subsequent fine denoising is used to solve this problem. The fine denoising results show that the photons below the ground have been removed as noise photons, while the object photons, such as tree canopy of mountain forests [Fig. 3(a1)] and building's rooftops [Fig. 3(a2-2)] above the ground surface, have been preserved as the signal photons. For the denoising results of urban areas [Fig. 3(a2-2) and (b2-3)], among the identified signal photons, it is obvious that there are relatively concentrated photons above the ground surface, most of which are rooftops of buildings or canopies of independent trees, and some photon clusters that may be noise that require further analysis. In addition, compared to PPC data with strong noise, data with weak noise contain a small number of noise photons, making it easy to identify the signal photons.

### B. Qualitative and Quantitative Comparison of Multiple Noise Reduction Methods

Fig. 4 plots the Gaussian histogram statistics and boxplot analysis on the elevation of the photons within each segmentation, which indicates the signal photons are centrally distributed in each segmentation, and these will help determine the major and minor axes of the elliptic filter kernel. For the elliptic filter kernel of the mountain forest area determined by automatic determination methods, the maximum, minimum, and mean of the semimajor axis are 20, 12, and 13 m, respectively, and the maximum, minimum, and mean of the semiminor axis are 15.8, 4.1, and 10.8 m, respectively.

Fig. 5 shows the comparison on the adaptive DBSCAN with other methods in PPC data with strong noise in mountain forest area. The results show that all these methods are capable of distinguishing signal photons on targets and noise photons, but the adaptive DBSCAN can more fully preserve the vertical structural features of ground and forest, as show in Fig. 5(a). Compared with the traditional DBSCAN and modified DBSCAN, the adaptive DBSCAN can identify more signal photon points in more complex terrain due to the adaptive elliptical

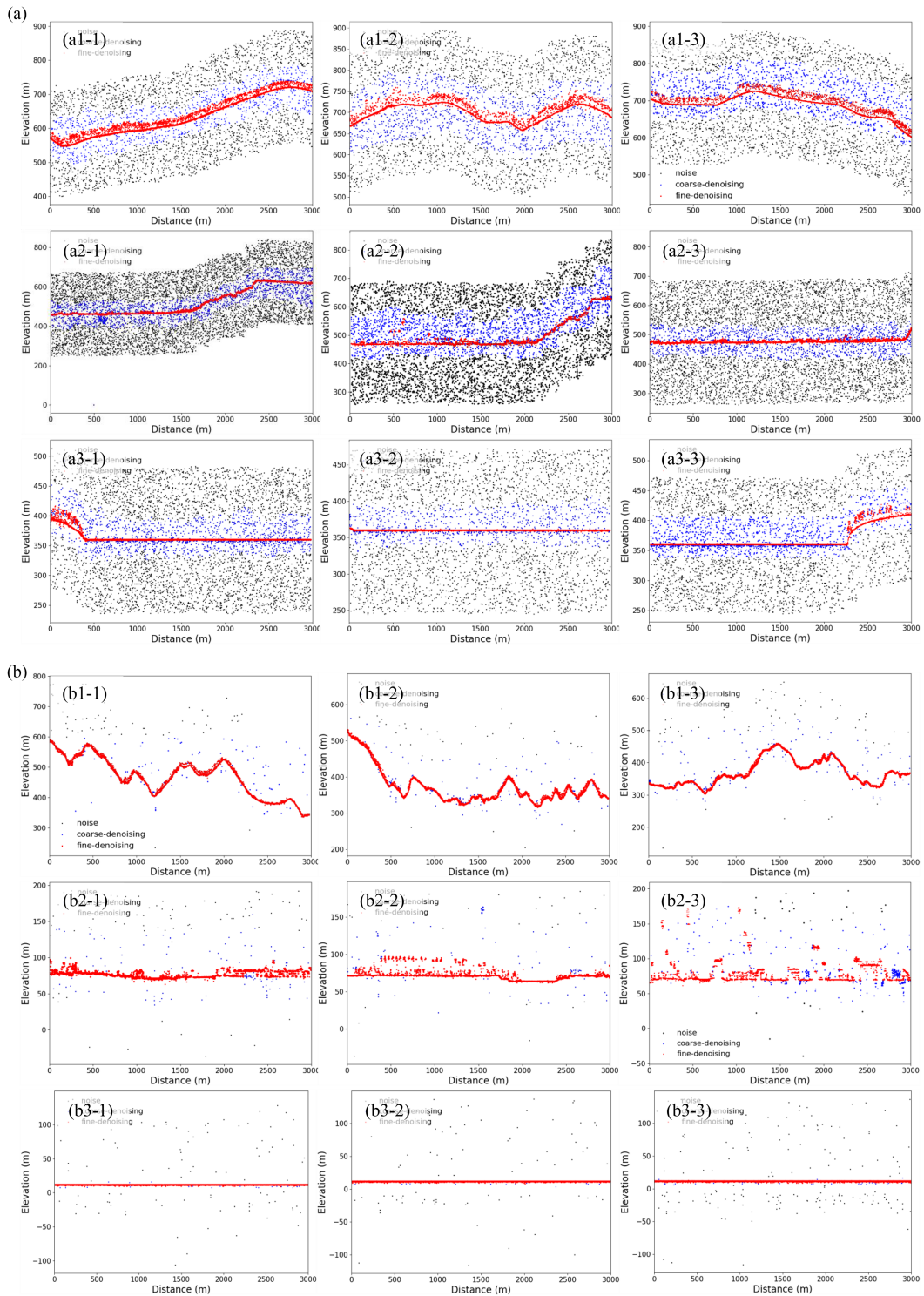


Fig. 3. Coarse and fine denoising for the photon point cloud of mountain forest, water, and urban area (black dots indicate noise, blue dots indicate the remain photons after coarse denoising, and red dot indicates the signal photons after fine denoising): (a1) forest, (a2) urban, and (a3) lake with strong noise; (b1) forest, (b2) urban, and (b3) lake with weak noise.

direction, which is calculated based on the terrain slope. In contrast, the DBSCAN and the modified DBSCAN are difficult to effectively detect weak photons of the forest canopy, and they may classify some signal photons on the forest canopy as noise photons. The insufficient number of correctly identified canopy

photons will limit subsequent applications, as shown in Fig. 5(b) and (c). The LDS cannot distinguish the noise photons around the ground and the canopy, making it difficult to completely remove the noise photons left near the ground, especially those below the ground, as shown in Fig. 5(d). The density of this

TABLE I  
QUANTITATIVE STATISTICS ON THE DENOISING PERFORMANCE OF ADAPTIVE DBSCAN, DBSCAN, MODIFIED DBSCAN, LDS, OPTICS, MODIFIED OPTICS, AND DRAGANN ON THE PPC DATA IN MOUNTAIN FOREST, URBAN, AND WATER AREAS

Methods	Evaluation	Forest		Urban		Lake		All		
		Strong	Weak	Strong	Weak	Strong	Weak	Maximum	Minimum	Mean
Adaptive DBSCAN	P	0.9679	0.9701	0.9499	0.9712	0.9696	0.9761	0.9761	0.9499	0.9675
	R	0.9715	0.9921	0.9746	0.9889	0.9916	0.9924	0.9924	0.9715	0.9852
	F	0.9778	0.9864	0.9561	0.9769	0.9789	0.9805	0.9864	0.9561	0.9761
DBSCAN	P	0.9531	0.9156	0.9146	0.9208	0.9462	0.9628	0.9628	0.9146	0.9355
	R	0.9179	0.9047	0.9745	0.9086	0.9866	0.9738	0.9866	0.9047	0.9444
	F	0.9587	0.9342	0.9358	0.9536	0.9773	0.9726	0.9773	0.9342	0.9554
Modified DBSCAN	P	0.9533	0.9355	0.9247	0.9519	0.9546	0.9642	0.9642	0.9247	0.9474
	R	0.9076	0.9588	0.9712	0.9589	0.9917	0.9796	0.9917	0.9076	0.9613
	F	0.9447	0.9362	0.9558	0.9593	0.9648	0.9733	0.9733	0.9557	0.9544
LDS	P	0.9255	0.9088	0.9209	0.9208	0.9358	0.9447	0.9447	0.9088	0.9261
	R	0.8989	0.9579	0.8848	0.9288	0.9767	0.9822	0.9822	0.8848	0.9382
	F	0.9318	0.9502	0.9045	0.9314	0.9771	0.9583	0.9771	0.9045	0.9422
	P	0.9254	0.9675	0.9314	0.9471	0.9006	0.9659	0.9675	0.9006	0.9397
OPTICS	R	0.9187	0.9867	0.9114	0.9592	0.9320	0.9581	0.9867	0.9114	0.9444
	F	0.9265	0.9421	0.9367	0.9478	0.9132	0.9604	0.9604	0.9132	0.9378
Modified OPTICS	P	0.9493	0.9581	0.9283	0.9369	0.9332	0.9702	0.9702	0.9283	0.9460
	R	0.9531	0.9824	0.9507	0.9661	0.9773	0.9807	0.9824	0.9507	0.9684
	F	0.9511	0.9631	0.9448	0.9679	0.9461	0.9785	0.9785	0.9448	0.9586
DRAGANN	P	0.9614	0.9679	0.9315	0.9084	0.9288	0.9489	0.9679	0.9084	0.9412
	R	0.9707	0.9867	0.9637	0.9703	0.9931	0.9795	0.9931	0.9637	0.9773
	F	0.9680	0.9847	0.9309	0.9337	0.9355	0.9687	0.9847	0.9309	0.9536

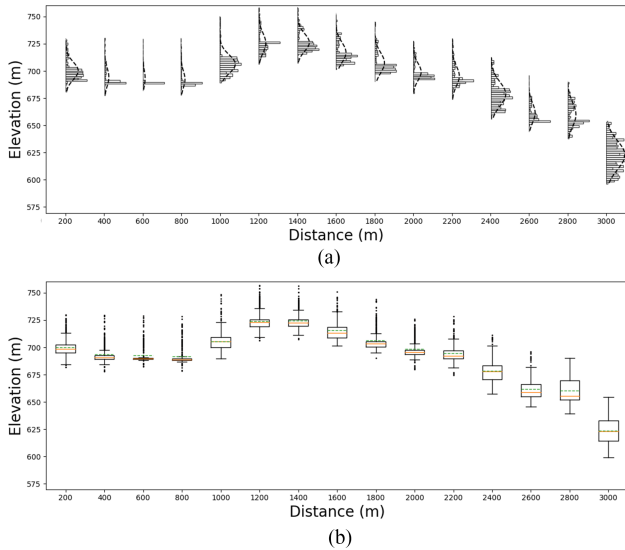


Fig. 4. Gaussian histogram statistics and boxplot analysis on the elevation of the photons within each segmentation on the strong noise in mountain forest area [corresponding to Fig. 1(a1-3)]: (a) histogram and Gaussian curve, and (b) boxplot analysis.

kind of noise photons differs from the density of peripheral noise photons and is obviously lower than the density of signal photons, and relatively close to the density of signal photons. Thus, this poses some challenges to the denoising algorithm. The OPTICS has improved upon the DBSCAN by being not

sensitive to input parameters, but like DBSCAN, it also cannot recognize some signal photons at the top of forest canopy, as shown in Fig. 5(e). A modified OPTICS has been improved, which changes the circular filter kernel to an ellipse, in order to be more suitable for the banded distribution of spaceborne PPC data. It can identify more signal points, especially the photons on the forest canopy above the ground points. Moreover, the number of noise points below the ground is obviously less than that of the traditional OPTICS, as shown in Fig. 5(f). The DRAGANN (result from ATL08 data products) also performs well, retaining the complete signal photons, but we found that some signals are lost in the area with sharply declining terrain, as shown on the far right of Fig. 5(g). In brief, the modified DBSCAN, the modified OPTICS, the DRAGANN, and the adaptive DBSCAN all perform well in fine denoising of the PPC data in mountain forest. However, the proposed adaptive DBSCAN performs well in various land-cover types with different terrain slopes.

Table I and Fig. 6 show the quantitative evaluation on the denoising performance of adaptive DBSCAN, DBSCAN, modified DBSCAN, LDS, OPTICS, modified OPTICS, and ATL08 results on the PPC data in mountain forest, urban, and water area. Indicators of R, P, and F are calculated using a manually selected reference data. The results show that the proposed adaptive DBSCAN performs the best accuracy on the PPC data with strong noise, the F values of PPC data with strong noise in the forest, urban, and water areas are 0.9778, 0.9561, and 0.9789, respectively, and the F values of PPC data with weak noise in these areas are 0.9864, 0.9769, and 0.9805, respectively.

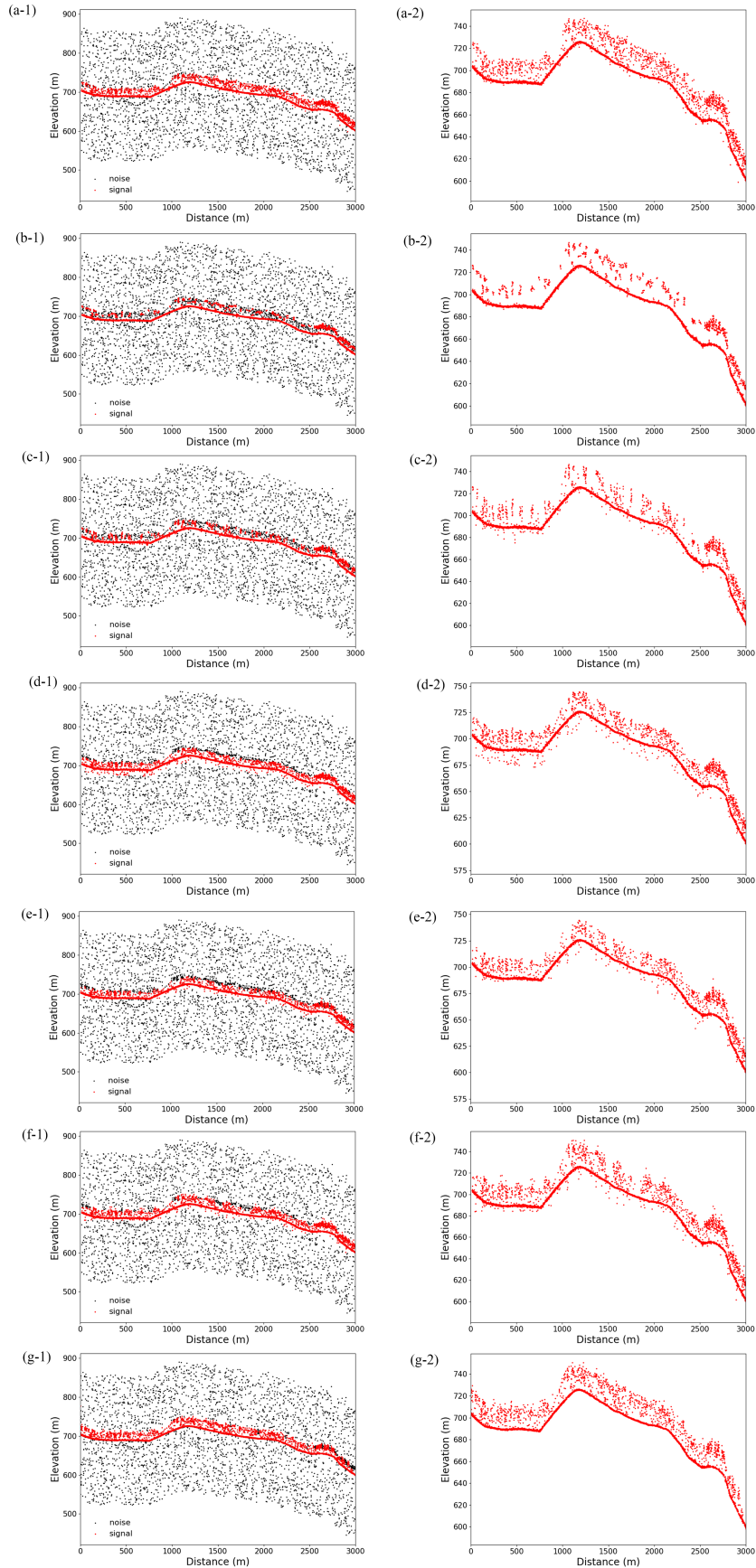


Fig. 5. Comparison of performance on signal identification (left) and signal photons (right) in PPC data with strong noise in mountain forest area [corresponding to Fig. 1(a1-3)]: (a) adaptive DBSCAN, (b) DBSCAN, (c) modified DBSCAN, (d) LDS, (e) OPTICS, (f) modified OPTICS, and (g) ATL08 result.

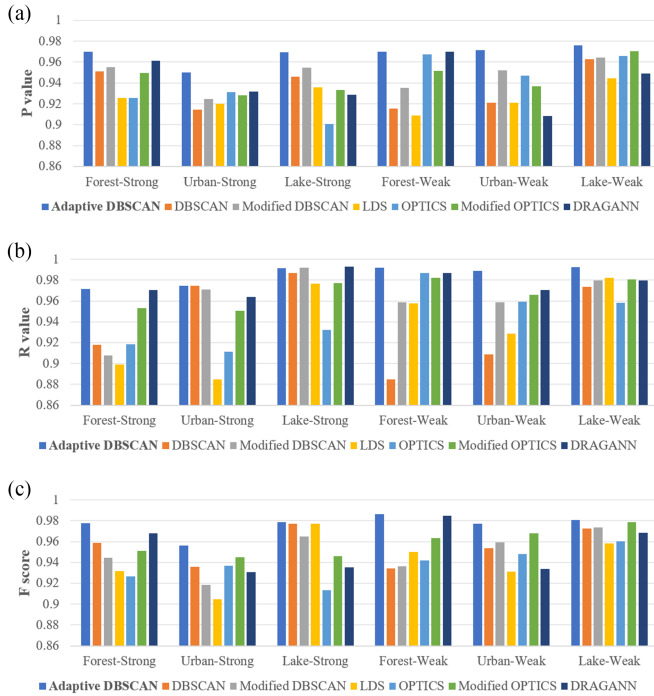


Fig. 6. Quantitative statistical histograms of denoising performance of adaptive DBSCAN, DBSCAN, modified DBSCAN, LDS, OPTICS, modified OPTICS, and ATL08 results in mountain forest, urban, and water areas: (a) P value, (b) R value, and (c) F score.

In the mountain forest area, the accuracy (P value) of adaptive DBSCAN in the case of strong and weak noise reaches 0.9679 and 0.9701, respectively, which is far higher than other methods. Compare to the PPC data with strong noise, all these methods can well remove the noise photons in the PPC data with weak noise, due to higher concentration in weak noise scenarios. In the urban and water areas, the performance of DBSCAN is close to that of the adaptive DBSCAN, possibly due to a shared characteristic of horizontally distributed ground objects in both types of data, that is both the surface of water and the rooftops of buildings are parallel to the ground. In the mountain forest area, the adaptive DBSCAN has obvious advantages than other methods, the reason is that it can adaptively change the direction of the search domain according to the slope of terrain. For the modified DBSCAN, modified OPTICS and DRAGANN also perform well with the mean of P value up to 0.9474, 0.9460, and 0.9412, respectively, only second to the adaptive DBSCAN, and surpassing traditional DBSCAN, traditional OPTICS and LDS, that with 0.9355, 0.9397, and 0.9261. The main reason is that the DBSCAN and OPTICS are less sensitive to input parameters, whereas other methods need to set appropriate parameters to achieve optimal denoising, which can be hard to apply to different types of data. And the modified DBSCAN and modified OPTICS change the circular filter kernel to an ellipse, which is more suitable for the higher density in the horizontal direction than vertical direction. On other hand, the DRAGANN performs well on extracting the ground and canopy signals. For the mean R, P, and F of the three types, the adaptive DBSCAN can get up to the maximum are 0.9852, 0.9675, and 0.9761, respectively;

followed by the DRAGANN with 0.9773, 0.9412, and 0.9536, the modified OPTICS with 0.9684, 0.9460, and 0.9586, and the modified DBSCAN with 0.9613, 0.9474, and 0.9544; and then the OPTICS with 0.9444, 0.9397, and 0.9378, and the DBSCAN with 0.9444, 0.9355, and 0.9554; the last one is the LDS with 0.9382, 0.9261, and 0.9422. In brief, these methods perform better on the PPC data with weak noise across the three land cover types than that of PPC data with strong noise, with the best performance in water areas. Moreover, the proposed adaptive DBSCAN demonstrates the best performance on the PPC data in all cases, with only a few cases showing comparable results to the DRAGANN and modified OPTICS, as shown in Fig. 6(a).

#### IV. CONCLUSION

The photon-counting laser altimeter can provide high-resolution elevation of natural and manmade terrain. Since the single-photon detection mechanism of instrument is sensitive to individual photons, the recorded PPC data are severely affected by the ambient noise, target feature, and instrument performance. It is particularly important to extract the signal photons on the ground surface before the subsequent applications. This article has presented an adaptive photonic detection method combined histogram statistic and boxplot analysis with modified DBSCAN to extract the signal photons. It can automatically determine the main parameters of the elliptic filter kernel (such as the major and minor axes and direction of the ellipse, and MinPts parameters) according to the data distribution characteristics. Experiments were performed on the strong and weak noise data from three typical land covers (i.e., mountain forest, urban, and water areas) obtained by ICESat-2/ATLAS. First, a coarse denoising was employed with Gaussian fitted histogram on the PPC data of ATL03 to remove over 90% of the noise photons. Second, a fine denoising based on adaptive DBSCAN was used to extract the real photon signals from remain photons, where the parameters for the elliptic filter kernel were automatically determined from a histogram statistics and boxplot analysis, and the local terrain slope. Finally, the performance was compared with other methods including LDS, traditional and modified DBSCAN, traditional and modified OPTICS, and DRAGANN. The results show that while all the methods can identify the signal photons on targets in complex terrain, the adaptive DBSCAN can more fully preserve the vertical structural features of ground objects in the complex terrain. Quantitative analysis using recall R, precision P, and harmonic mean of recall and precision F-score also indicates that the adaptive DBSCAN in the mean R, P, and F of the three types can get up to the maximum are 0.9852, 0.9675, and 0.9761, respectively; followed by the DRAGANN with 0.9773, 0.9412, and 0.9536, the modified OPTICS with 0.9684, 0.9460, and 0.9586, and the modified DBSCAN with 0.9613, 0.9474, and 0.9544; and then the OPTICS with 0.9444, 0.9397, and 0.9378, and the DBSCAN with 0.9444, 0.9355, and 0.9554; the last one is the LDS with 0.9382, 0.9261, and 0.9422.

The proposed signal photon detection method can automatically determine the main parameters according to topographic data situation and has the best performance compared to some other classical methods, and it provides an alternative and

robustness approach for the rapid and accurate processing of PPC data on complex terrain. The main contributions of this article are the automatic determination of major and minor axes based on the density situation of PPC data to avoid the trouble of empirical models, and adaptive selection of direction according to the local terrain slope from the PPC data to avoid the high consumption of traversal search.

#### ACKNOWLEDGMENT

The authors thank the National Snow and Ice Data Center for providing the ICESat-2 data used in this article. We also would like to thank our anonymous reviewers for their constructive suggestion to improve the quality of this article.

#### REFERENCES

- [1] X. Wang, X. Cheng, P. Gong, H. Huang, Z. Li, and X. Li, "Earth science applications of ICESat/GLAS: A review," *Int. J. Remote Sens.*, vol. 32, no. 23, pp. 8837–8864, Aug. 2011, doi: [10.1080/01431161.2010.547533](https://doi.org/10.1080/01431161.2010.547533).
- [2] J. U. H. Eitel et al., "Beyond 3-D: The new spectrum of LiDAR applications for earth and ecological sciences," *Remote Sens. Environ.*, vol. 186, pp. 372–392, Dec. 2016, doi: [10.1016/j.rse.2016.08.018](https://doi.org/10.1016/j.rse.2016.08.018).
- [3] P. Dabney et al., "The slope imaging multi-polarization photon-counting LiDAR: Development and performance results," in *Proc. IEEE Int. Geosci. Remote Sens. Symp.*, 2010, pp. 653–656, doi: [10.1109/IGARSS.2010.5650862](https://doi.org/10.1109/IGARSS.2010.5650862).
- [4] J. Rosette, C. Field, R. Nelson, P. DeCola, and B. Cook, "A new photon-counting LiDAR system for vegetation analysis," in *Proc. Silvilaser*, 2010, pp. 16–19.
- [5] M. McGill, T. Markus, V. S. Scott, and T. Neumann, "The multiple altimeter beam experimental LiDAR (MABEL): An airborne simulator for the ICESat-2 mission," *J. Atmos. Ocean Technol.*, vol. 30, no. 2, pp. 345–352, Feb. 2013, doi: [10.1175/JTECH-D-12-00076.1](https://doi.org/10.1175/JTECH-D-12-00076.1).
- [6] J. Zhang, J. Kerekes, B. Csatho, T. Schenk, and R. Wheelwright, "A clustering approach for detection of ground in micropulse photon-counting LiDAR altimeter data," in *Proc. IEEE Geosci. Remote Sens. Symp.*, 2014, pp. 177–180, doi: [10.1109/IGARSS.2014.6946385](https://doi.org/10.1109/IGARSS.2014.6946385).
- [7] A. Swatantran, H. Tang, T. Barrett, P. DeCola, and R. Dubayah, "Rapid, high-resolution forest structure and terrain mapping over large areas using single photon LiDAR," *Sci. Rep.*, vol. 6, Jun. 2016, Art. no. 28277, doi: [10.1038/srep28277](https://doi.org/10.1038/srep28277).
- [8] T. Markus et al., "The ice, cloud, and land elevation satellite-2 (ICESat-2): Science requirements, concept, and implementation," *Remote Sens. Environ.*, vol. 190, pp. 260–273, Mar. 2017, doi: [10.1016/j.rse.2016.12.029](https://doi.org/10.1016/j.rse.2016.12.029).
- [9] M. Krainak, A. Yu, G. Yang, S. Li, and X. Sun, "Photon-counting detectors for space-based laser receivers," *Proc. SPIE Int. Soc. Opt. Eng.*, vol. 7780, Aug. 2010, Art. no. 7608, doi: [10.1117/12.864025](https://doi.org/10.1117/12.864025).
- [10] J. Kerekes et al., "First principles modeling for LiDAR sensing of complex ice surfaces," in *Proc. IEEE Int. Geosci. Remote Sens. Symp.*, 2012, pp. 3241–3244, doi: [10.1109/IGARSS.2012.6350733](https://doi.org/10.1109/IGARSS.2012.6350733).
- [11] S. C. Popescu et al., "Photon counting LiDAR: An adaptive ground and canopy height retrieval algorithm for ICESat-2 data," *Remote Sens. Environ.*, vol. 208, pp. 154–170, Apr. 2018, doi: [10.1016/j.rse.2018.02.019](https://doi.org/10.1016/j.rse.2018.02.019).
- [12] L. A. Magruder, M. E. Wharton, K. D. Stout, and A. L. Neuenschwander, "Noise filtering techniques for photon-counting LiDAR data," *Proc. SPIE Defense, Secur., Sens., Laser Radar Technol. Appl.*, vol. XVII, May 2012, Art. no. 83790Q, doi: [10.1117/12.919139](https://doi.org/10.1117/12.919139).
- [13] M. Awadallah, S. Ghannam, L. Abbott, and A. M. Ghanem, "Active contour models for extracting ground and forest canopy curves from discrete laser altimeter data," in *Proc. 13th Int. Conf. LiDAR Appl. Assessing Forest Ecosyst.*, 2013, Art. no. 111.
- [14] H. Tang, A. Swatantran, T. Barrett, P. DeCola, and R. Dubayah, "Voxel-based spatial filtering method for canopy height retrieval from airborne single-photon LiDAR," *Remote Sens.*, vol. 8, no. 9, Sep. 2016, Art. no. 771, doi: [10.3390/rs8090771](https://doi.org/10.3390/rs8090771).
- [15] K. M. Brunt, T. A. Neumann, K. M. Walsh, and T. Markus, "Determination of local slope on the Greenland ice sheet using a multibeam photon-counting LiDAR in preparation for the ICESat-2 mission," *IEEE Geosci. Remote Sens. Lett.*, vol. 11, no. 5, pp. 935–939, May 2014, doi: [10.1109/LGRS.2013.2282217](https://doi.org/10.1109/LGRS.2013.2282217).
- [16] M. S. Moussavi, W. Abdalati, T. Scambos, and A. Neuenschwander, "Applicability of an automatic surface detection approach to micro-pulse photon-counting LiDAR altimetry data: Implications for canopy height retrieval from future ICESat-2 data," *Int. J. Remote Sens.*, vol. 35, no. 13, pp. 5263–5279, Jul. 2014, doi: [10.1080/01431161.2014.939780](https://doi.org/10.1080/01431161.2014.939780).
- [17] K. M. Brunt et al., "MABEL photon-counting laser altimetry data in Alaska for ICESat-2 simulations and development," *Cryosphere*, vol. 10, no. 4, pp. 1707–1719, Aug. 2016, doi: [10.5194/tc-10-1707-2016](https://doi.org/10.5194/tc-10-1707-2016).
- [18] D. Gwenzi, M. A. Lefsky, V. P. Suchdeo, and D. J. Harding, "Prospects of the ICESat-2 laser altimetry mission for savanna ecosystem structural studies based on airborne simulation data," *ISPRS J. Photogrammetry Remote Sens.*, vol. 118, pp. 68–82, Aug. 2016, doi: [10.1016/j.isprsjprs.2016.04.009](https://doi.org/10.1016/j.isprsjprs.2016.04.009).
- [19] X. Zhu, S. Nie, C. Wang, X. Xi, and Z. Hu, "A ground elevation and vegetation height retrieval algorithm using micro-pulse photon-counting LiDAR data," *Remote Sens.*, vol. 10, no. 12, Dec. 2018, Art. no. 1962, doi: [10.3390/rs10121962](https://doi.org/10.3390/rs10121962).
- [20] S. Nie et al., "Estimating the vegetation canopy height using micro-pulse photon-counting LiDAR data," *Opt. Exp.*, vol. 26, no. 10, pp. A520–A540, May 2018, doi: [10.1364/oe.26.00a520](https://doi.org/10.1364/oe.26.00a520).
- [21] S. Xia, C. Wang, X. Xi, S. Luo, and H. Zeng, "Point cloud filtering and tree height estimation using airborne experiment data of ICESat-2," *J. Remote Sens.*, vol. 18, no. 6, pp. 1199–1207, Feb. 2014, doi: [10.11834/jrs.20144029](https://doi.org/10.11834/jrs.20144029).
- [22] B. Chen et al., "Ground and top of canopy extraction from photon-counting LiDAR data using local outlier factor with ellipse searching area," *IEEE Geosci. Remote Sens. Lett.*, vol. 16, no. 9, pp. 1447–1451, Sep. 2019, doi: [10.1109/LGRS.2019.2899011](https://doi.org/10.1109/LGRS.2019.2899011).
- [23] U. C. Herzfeld et al., "Algorithm for detection of ground and canopy cover in micropulse photon-counting LiDAR altimeter data in preparation for the ICESat-2 mission," *IEEE Trans. Geosci. Remote Sens.*, vol. 52, no. 4, pp. 2109–2125, Apr. 2014, doi: [10.1109/TGRS.2013.2258350](https://doi.org/10.1109/TGRS.2013.2258350).
- [24] X. Wang, Z. Pan, and C. Glennie, "A novel noise filtering model for photon-counting laser altimeter data," *IEEE Geosci. Remote Sens. Lett.*, vol. 13, no. 7, pp. 947–951, Jul. 2016, doi: [10.1109/LGRS.2016.2555308](https://doi.org/10.1109/LGRS.2016.2555308).
- [25] J. Zhang and J. Kerekes, "An adaptive density-based model for extracting surface returns from photon-counting laser altimeter data," *IEEE Geosci. Remote Sens. Lett.*, vol. 12, no. 4, pp. 726–730, Apr. 2015, doi: [10.1109/LGRS.2014.2360367](https://doi.org/10.1109/LGRS.2014.2360367).
- [26] J. Huang, Y. Xing, H. You, L. Qin, J. Tian, and J. Ma, "Particle swarm optimization-based noise filtering algorithm for photon cloud data in forest area," *Remote Sens.*, vol. 11, no. 8, Apr. 2019, Art. no. 980, doi: [10.3390/rs11080980](https://doi.org/10.3390/rs11080980).
- [27] M. Ankerst, M. M. Breunig, H.-P. Kriegel, and J. Sander, "OPTICS: Ordering points to identify the clustering structure," *ACM SIGMOD Rec.*, vol. 28, no. 2, pp. 49–60, Jun. 1999.
- [28] X. Zhu et al., "A noise removal algorithm based on OPTICS for photon-counting LiDAR data," *IEEE Geosci. Remote Sens. Lett.*, vol. 18, no. 8, pp. 1471–1475, Aug. 2021, doi: [10.1109/LGRS.2020.3003191](https://doi.org/10.1109/LGRS.2020.3003191).
- [29] T. A. Neumann et al., "ATLAS/ICESat-2 L2A global geolocated photon data, version 6," Boulder, Colorado USA. NASA National Snow and Ice Data Center Distributed Active Archive Center, 2023, doi: [10.5067/ATLAS/ATL03.006](https://doi.org/10.5067/ATLAS/ATL03.006).
- [30] D. Gwenzi, M. A. Lefsky, V. P. Suchdeo, and D. J. Harding, "Prospects of the ICESat-2 laser altimetry mission for savanna ecosystem structural studies based on airborne simulation data," *ISPRS J. Photogrammetry Remote Sens.*, vol. 118, pp. 68–82, May 2016, doi: [10.1016/j.isprsjprs.2016.04.009](https://doi.org/10.1016/j.isprsjprs.2016.04.009).
- [31] A. Neuenschwander and K. Pitts, "The ATL08 land and vegetation product for the ICESat-2 Mission," *Remote Sens. Environ.*, vol. 221, pp. 247–259, Feb. 2019, doi: [10.1016/j.rse.2018.11.005](https://doi.org/10.1016/j.rse.2018.11.005).
- [32] H. Xie et al., "A comparison and review of surface detection methods using MBL, MABEL, and ICESat-2 photon-counting laser altimetry data," *IEEE J. Sel. Topics Appl. Earth Observ. Remote Sens.*, vol. 14, pp. 7604–7623, Jul. 2021, doi: [10.1109/JSTARS.2021.3094195](https://doi.org/10.1109/JSTARS.2021.3094195).
- [33] Y. Li, H. Fu, J. Zhu, and C. Wang, "A filtering method for ICESat-2 photon point cloud data based on relative neighboring relationship and local weighted distance statistics," *IEEE Geosci. Remote Sens. Lett.*, vol. 18, no. 11, pp. 1891–1895, Nov. 2021, doi: [10.1109/LGRS.2020.3011215](https://doi.org/10.1109/LGRS.2020.3011215).
- [34] M. Ester, H. P. Kriegel, J. Sander, and X. Xu, "A density-based algorithm for discovering clusters in large spatial databases with noise," in *Proc. 2nd Int. Conf. Knowl. Discov. Data Mining*, 1996, pp. 226–231.
- [35] F. Xie, G. Yang, R. Shu, and M. Li, "An adaptive directional filter for photon counting LiDAR point cloud data," *J. Infrared Millimeter THz Waves*, vol. 36, no. 1, Mar. 2017, Art. no. 107, doi: [10.11972/j.issn.1001-9014.2017.01.019](https://doi.org/10.11972/j.issn.1001-9014.2017.01.019).

- [36] Z. Zhang, X. Liu, Y. Ma, N. Xu, W. Zhang, and S. Li, "Signal photon extraction method for weak beam data of ICESat-2 using information provided by strong beam data in mountainous areas," *Remote Sens.*, vol. 13, no. 5, Feb. 2021, Art. no. 863, doi: [10.3390/rs13050863](https://doi.org/10.3390/rs13050863).
- [37] J. Lao et al., "Retrieving building height in urban areas using ICESat-2 photon-counting LiDAR data," *Int. J. Appl. Earth Observ. Geoinf.*, vol. 104, Dec. 2021, Art. no. 102596, doi: [10.1016/j.jag.2021.102596](https://doi.org/10.1016/j.jag.2021.102596).
- [38] J. Lao et al., "A new denoising method for photon-counting LiDAR data with different surface types and observation conditions," *Int. J. Digit. Earth*, vol. 16, no. 1, pp. 1551–1567, Apr. 2023, doi: [10.1080/17538947.2023.2203952](https://doi.org/10.1080/17538947.2023.2203952).
- [39] L. He, Y. Pang, Z. Zhang, X. Liang, and B. Chen, "ICESat-2 data classification and estimation of terrain height and canopy height," *Int. J. Appl. Earth Observ. Geoinf.*, vol. 118, Feb. 2023, Art. no. 103233, doi: [10.1016/j.jag.2023.103233](https://doi.org/10.1016/j.jag.2023.103233).
- [40] Y. Ma et al., "Photon-counting LiDAR: An adaptive signal detection method for different land cover types in coastal areas," *Remote Sens.*, vol. 11, no. 4, Feb. 2019, Art. no. 471, doi: [10.3390/rs11040471](https://doi.org/10.3390/rs11040471).
- [41] W. Meng, J. Li, K. Zhang, C. Liu, and Q. Tang, "Denoising of ICESat-2 surface point data based on improved DBSCAN algorithm and accuracy evaluation," *Ocean Bull.*, vol. 40, no. 6, pp. 675–682, Mar. 2021, doi: [10.11840/j.issn.1001-6392.2021.06.008](https://doi.org/10.11840/j.issn.1001-6392.2021.06.008).
- [42] G. Zhang, W. Lian, S. Li, H. Cui, M. Jing, and Z. Chen, "A self-adaptive denoising algorithm based on genetic algorithm for photon-counting LiDAR data," *IEEE Geosci. Remote Sens. Lett.*, vol. 19, Mar. 2021, Art. no. 6501405, doi: [10.1109/LGRS.2021.3067609](https://doi.org/10.1109/LGRS.2021.3067609).
- [43] T. Neumann et al., "The ice, cloud, and land elevation satellite-2 mission: A global geolocated photon product derived from the advanced topographic laser altimeter system," *Remote Sens. Environ.*, vol. 233, Nov. 2019, Art. no. 11325, doi: [10.1016/j.rse.2019.111325](https://doi.org/10.1016/j.rse.2019.111325).
- [44] M. E. Brown et al., "Applications for ICESat-2 data: From NASA's early adopter program," *IEEE Geosci. Remote Sens. Mag.*, vol. 4, no. 4, pp. 24–37, Dec. 2016, doi: [10.1109/MGRS.2016.2560759](https://doi.org/10.1109/MGRS.2016.2560759).
- [45] M. F. Jasinski, J. D. Stoll, W. B. Cook, M. Ondrusek, E. Stengel, and K. Brunt, "Inland and near-shore water profiles derived from the high-altitude multiple altimeter beam experimental LiDAR (MABEL)," *J. Coastal Res.*, vol. 76, pp. 44–55, Apr. 2016, doi: [10.2112/SI76-005](https://doi.org/10.2112/SI76-005).



**Xiangfeng Liu** received the B.S. degree in geographic information system from the Information Engineering University, Zhengzhou, China, in 2008, the M.S. degree in cartography and geographic information engineering from the Liaoning Technical University, Fuxin, China, in 2011, and the Ph.D. degree in cartography and geographic information engineering from the Tongji University, Shanghai, China, in 2017.

He is currently a Research Assistant with the Shanghai Institute of Technical Physics, Chinese Academy of Sciences, Shanghai, China. His research

interests include calibration and application of active and passive remote sensing.



**Zhenhua Wang** received the B.S. degree in geographical science from the School of Geographical Sciences, Yantai Normal University, Yantai, China, in 2004, the M.S. degree in geochemistry from the Chinese Academy of Sciences, Beijing, China, in 2007, and the Ph.D. degree in cartography and geographic information engineering from the Tongji University, Shanghai, China, in 2010.

She is currently an Associate Professor with the College of Information Technology, Shanghai Ocean University, Shanghai, China. Her research interests

include spatial data analysis, data quality control, and deep learning.



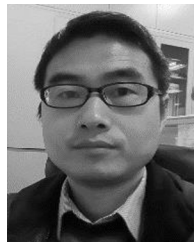
**Shixian Chen**, photograph and biography not available at the time of publication.



**Fengxiang Wang** received the B.S. degree in surveying and mapping engineering from Tongji University, Shanghai, China, in 2012, and the M.S. degree in cartography and geographic information engineering from Tongji University, Shanghai, China, in 2015.

She is currently a Research Assistant with the Shanghai Institute of Technical Physics, Chinese Academy of Sciences, Shanghai, China. Her research interests include space LiDAR data processing and sensor calibration.

**Xiaowei Chen**, photograph and biography not available at the time of publication.



**Weiming Xu** received the B.S. degree in physics from the Beijing Normal University, Beijing, China, in 2000, and the Ph.D. degree in physical electricity from the Shanghai Institute of Technical Physics, Chinese Academy of Sciences (CAS), Shanghai, China, in 2005.

He is currently a Professor with the Shanghai Institute of Technical Physics, CAS. His research interests include development of space optoelectronic instruments.

Dr. Xu is the Director Designer of the laser 3-D imaging sensor of Chang'e-3 Lunar exploration lander, and Tianwen-1 Mars surface composition detector, and so on. He was the recipient of the Jeoujang Jaw Outstanding Science Award for Young and Middle-aged Scientists, etc.



**Rong Shu** received the B.S. degree in mechanical and electrical integration from the Hefei University of Technology, Hefei, China, in 1992, and the Ph.D. degrees in physical electronics from the Graduate School of the Chinese Academy of Sciences, Shanghai, China, in 2006.

He is currently a Senior Researcher with the Shanghai Institute of Technical Physics, CAS, Shanghai, China. His research interests include space active optoelectronics technology.

Dr. Shu has led the payload development tasks in a number of national major space missions, such as lunar exploration missions, Tianwen-1 Mars mission, high-resolution Earth observation system projects, and so on. He also served as the Deputy Director of China's first quantum scientific experiment satellite (Mozi Satellite). He was the recipient of 10 national and provincial awards, as well as an international award, i.e., 2018 Cleveland Prize.